Scilight

Journal of Innovations in Materials and Manufacturing Engineering
https://www.sciltp.com/journals/jimme

Article

Check for updates

Effects of Key Processing Parameters on Multi-Objective Performance of MEX Fabricated PETG Parts

Tenglong Liu, Hui Wang *, Yunfu Luo, Ye Wang, Hao Li, Baochuan Tan, Yue Pan and Lizi Liu

College of Mechanical Engineering, Chongqing Three Gorges University, Chongqing 404130, China
* Correspondence: wanghui@sanxiau.edu.cn

How To Cite: Liu, T.; Wang, H.; Luo, Y.; et al. Effects of Key Processing Parameters on Multi-Objective Performance of MEX Fabricated PETG Parts. *Journal of Innovations in Materials and Manufacturing Engineering* **2026**, *1*(1), 6. https://doi.org/10.53941/jimme.2026.100006

Received: 26 March 2026
Revised: 28 April 2026
Accepted: 12 May 2026
Published: 14 May 2026

Abstract: With the rapid advancement of additive manufacturing, Material Extrusion (MEX) has become widely adopted due to its low cost and high process flexibility. However, optimizing MEX processing parameters to balance multiple performance objectives in engineered polymers such as PETG remains a critical challenge. To collaboratively enhance tensile strength, printing efficiency, and material usage efficiency (MUE) of MEX-printed PETG parts, this study employed a multi-objective optimization using the desirability function method. Using single-factor and Taguchi orthogonal experiments, along with ANOVA and multiple linear regression, the coupling mechanisms among infill density, layer height, infill pattern, perimeter shells, and printing temperature for tensile strength, printing time, and MUE were rigorously characterized to elucidate their underlying interdependencies. Based on the established empirical prediction models for tensile strength, printing time, and MUE, the optimal parameter combination was identified as 52% infill density, 0.25 mm layer height, a grid infill pattern, 5 perimeter shells, and 250 °C printing temperature. Experimental validation yielded a measured tensile strength of 38.81 MPa, with a deviation of less than 1% from the predicted value. Furthermore, the printing time and MUE met the design objectives with excellent stability. The proposed MUE evaluation and multi-objective optimization framework provides essential theoretical and technical support for the efficient and economical manufacturing of MEX-printed PETG functional components.

Keywords: MEX; PETG; Taguchi method; mechanical properties; tensile strength

1. Introduction

Against the backdrop of the global low-carbon transition and green manufacturing-driven industrial development, advanced manufacturing technology has become a key pillar for achieving efficient resource utilization and promoting industrial upgrading, ushering in unprecedented development opportunities [1]. In the late 20th century, S. Scott Crump, while using a hot glue gun to customize a toy for his daughter, conceived the forming principle of layer-by-layer deposition, which led to the development of Material Extrusion (MEX) technology [2]. This innovative attempt, rooted in daily needs, completely revolutionized the production method of traditional subtractive manufacturing, and the core characteristics of MEX technology—near-net shaping and on-demand deposition—are highly aligned with the development demands of green manufacturing for waste reduction and efficient resource utilization [3,4]. The specific process of this technology is illustrated in Figure 1, including CAD modeling, slicing processing, layer-by-layer deposition printing, and post-processing steps such as support removal [5,6].

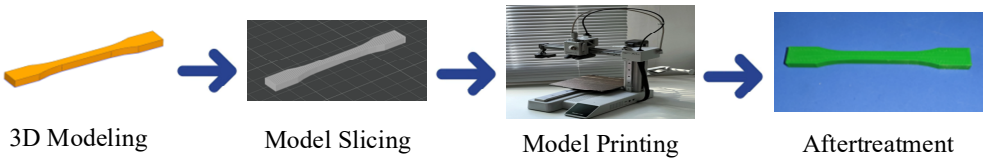

Figure 1. Flow chart of MEX additive manufacturing.

In recent years, due to its advantages such as low equipment costs, ease of operation, and broad material compatibility, MEX technology has been widely used in various fields, including aerospace, automotive components, and consumer goods [7–11]. Among them, Polyethylene terephthalate glycol-modified (PETG), as a high-performance engineering polymer, integrates favorable tensile strength, toughness, and molding stability. Consequently, PETG has emerged as an ideal and mainstream material for MEX technology [12–19]. To fully exploit the superior properties of PETG, a systematic optimization of the printing process is required. This aims to achieve the dual objectives of high material utilization and cost-effectiveness while ensuring robust mechanical performance [20–22].

Although scholars have conducted extensive research on process parameter optimization for commonly used polymers in MEX, existing studies still exhibit significant limitations. On the one hand, most adopt single-factor experiments or focus on the independent effects of two or three types of printing parameters, overlooking the coupling effects among multiple parameters and failing to reveal their complex interdependencies deeply.

For instance, Popović et al. optimized the nozzle temperature and printing speed of MEX-printed PLA tensile specimens to meet industrial customization needs, identifying 190 °C and 40 mm/min as the optimal parameters based on roughness and tensile tests [23]. Özen et al. focused on the mechanical characterization of MEX-printed polymers by comparing four tensile specimen geometries. By combining finite element analysis with tensile testing, they revealed the influence of slicing parameters on failure locations and proposed simplified test specifications for the effective mechanical properties of 3D-printed structures [24]. Lakshman Sri et al. determined the optimal strength process combinations for PETG and PA6 by adjusting MEX printing parameters and utilized Scanning Electron Microscopy (SEM) to reveal the micro-forming mechanisms [25]. Vidakis et al. prepared five common 3D-printed thermoplastics via the MEX process to systematically study their tensile strain rate sensitivity. Combined with SEM fracture analysis and EM algorithms, they revealed the effects of strain rate on mechanical properties and fracture behavior [26]. Nugroho et al. found through three-point bending tests that the flexural strength of MEX-printed PLA increases with layer height, reaching an optimum at 0.5 mm, noting that thicker layers facilitate interlayer bonding while thinner layers are prone to delamination [27]. Loskot et al. systematically characterized the impact of MEX printing speed on the microstructure, surface quality, and micromechanical properties of PETG, specifying that the appropriate printing speed should not exceed 60 mm/s [28].

On the other hand, some studies have begun to consider printing energy efficiency or multi-parameter coupling, but have yet to achieve a correlation and synergistic analysis of the two. Valvez et al. investigated the compression performance of MEX-molded PLA parts by exploring nozzle temperature and printing speed, identifying 190 °C and 40 mm/min as the optimal combination, while 190 °C and 80 mm/min could be selected when prioritizing efficiency [29]. Bembenek et al. examined the printing temperature, orientation, layer height, and infill percentage of PLA and PETG parts, proposing Specific Tensile Strength (STS) to eliminate evaluation bias caused by specimen weight [30]. Luo et al. proposed a dual-nozzle selective reinforcement process that enhances printing flexibility and parameter adjustment efficiency, reducing manufacturing costs and improving process efficiency through local reinforcement [31]. Kechagias et al. studied the effects of nozzle temperature, printing speed, and layer height on the specific strength and specific energy consumption of MEX-printed PEEK parts. Through ANOVA and second-order models, they identified key parameters and obtained an optimized parameter combination that balances high mechanical strength with low energy consumption [32].

Currently, research on MEX process optimization has explored various materials regarding mechanical properties, printing parameters, and strain rates [25,26]. However, existing research still primarily focuses on single-objective mechanical property optimization, lacking a unified integration of efficiency and cost in actual production, which makes it difficult to form a comprehensive optimization system. Although some studies have attempted to incorporate specimen strength and energy consumption into synergistic optimization, the energy indicators used are often too theoretical and abstract, detaching from actual industrial application needs and lacking engineering practicality [32–34]. Crucially, simultaneous multi-dimensional optimization remains underexplored. Given the pain points of MEX parts, such as weak interlayer bonding, high porosity, and insufficient stability, there is a lack of optimized parameters that synergistically consider mechanical performance, printing efficiency, and material cost, hindering the practical implementation in industrial and general scenarios. Therefore, there is an urgent

need to establish a scientific and economical multi-objective optimization system to address the key issues of insufficient printing cost quantification and inadequate analysis of parameter coupling in the MEX process.

Consequently, this study focuses on PETG parts fabricated via the MEX process, selecting printing temperature, infill density, layer height, infill pattern, and perimeter shells as key process parameters. With tensile strength, printing time, and material usage efficiency (MUE) as optimization objectives, the influence of parameters was systematically investigated through orthogonal testing and ANOVA, leading to a multi-objective optimization. Ultimately, a synergistic balance between mechanical performance, molding efficiency, and material economy was achieved [35,36].

2. Materials and Equipment

In this study, commercially available pure PETG filament provided by Bambu Lab was utilized. PETG, a transparent amorphous copolyester, exhibits exceptional toughness and formability, with a measured filament diameter of 1.75 ± 0.03 mm. According to the manufacturer's technical data sheet, the PETG has a density of 1.25 g/cm^3 (tested per ISO 1183) and a glass transition temperature of 69 °C. The recommended printing parameters include a nozzle temperature of 230–260 °C and a heat bed temperature of 65–75 °C, which are fully consistent with the parameter ranges selected for this study.

For each parameter combination, three parallel tensile specimens were fabricated. The specimen dimensions were strictly determined according to the GB/T 1040.1-2018 standard (Plastics—Determination of tensile properties—Part 1: General principles), as illustrated in Figure 2a. Tensile testing was performed using a JHY-5000 universal testing machine with a constant crosshead speed of 5 mm/min. As illustrated in Figure 2, (a) depicts the geometric dimensions of the tensile specimen; while (b) shows the as-fabricated samples used for orthogonal tests and mechanical measurements.

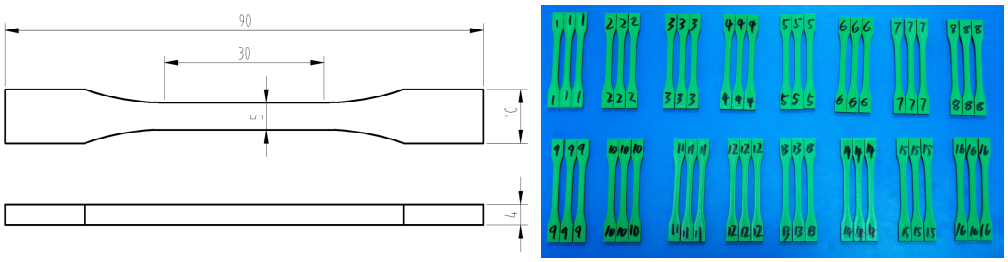

Figure 2. Schematic of tensile specimen geometry and dimensions (**a**) and photograph of as-fabricated test samples (**b**).

As illustrated in Figure 3, the additive manufacturing process was performed using a Bambu Lab X1-Carbon Combo 3D printer equipped with a 0.4 mm diameter stainless steel nozzle. All test specimens were fabricated from G-code files generated via the dedicated Bambu Studio slicer software. Subsequently, tensile tests were performed on a JHY-5000 universal testing machine, wherein the printed specimens were clamped in tensile grips and loaded at a constant rate of 5 mm/min until fracture, in accordance with relevant standard specifications [37,38].

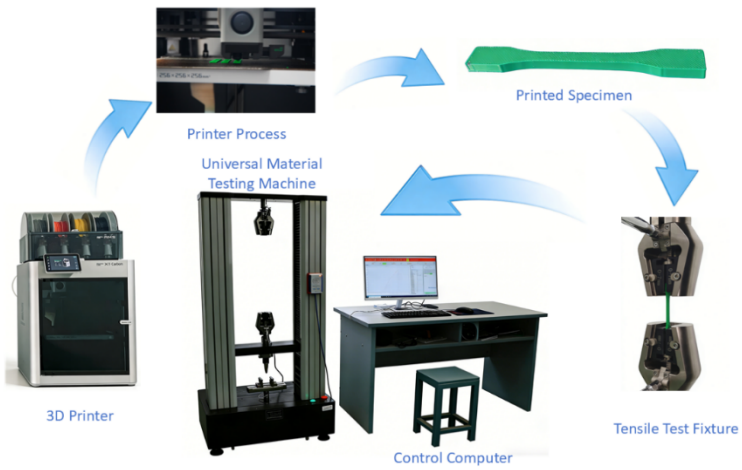

Figure 3. Flowchart of 3D printing fabrication and mechanical testing.

3. Methodology

3.1. Single-Factor Experiments

Building upon extant research regarding the influence of Material Extrusion (MEX) process parameters on the mechanical integrity of printed parts, and considering the practical tensile and flexural loading conditions encountered in industrial applications, five critical parameters—namely infill density, layer height, infill pattern, number of perimeter shells, and printing temperature—were selected for in-depth investigation [26,27,32,39].

The physical significance and research necessity of the selected parameters are as follows: infill density directly determines material usage and internal support strength; layer height significantly influences printing efficiency while concurrently modulating interlayer bonding strength by altering the contact area; printing temperature, as the most sensitive thermal factor for PETG, controls melt fluidity and the degree of interlayer fusion, which directly affects the interlayer strength of the molded material; perimeter shells are a critical geometric parameter due to their high load-bearing proportion under tensile conditions; and the infill pattern significantly affects the final failure mode of the parts by altering internal load transfer paths. Furthermore, the influence of infill patterns on the mechanical performance of printed parts has been confirmed in extensive prior research, revealing significant performance differences among various patterns. Therefore, four typical infill patterns, which are the most widely applied in the MEX process and commonly adopted in literature, were selected as the focus of this investigation [3,22].

To compensate for the limitations of single-factor experiments, which analyze only individual variables, this study implemented a systematic approach integrating single-factor pre-experiments, Taguchi orthogonal (Taguchi-OA) testing, and multi-objective optimization. The levels for the orthogonal tests were determined based on the fusion characteristics of PETG and mechanical response laws. To ensure the scientific validity of the experimental design and avoid deviations from sensitive performance intervals, single-factor experiments were first conducted to clarify the influence trends of each key parameter. This provided a reliable basis for defining the parameter ranges in the subsequent multi-factor orthogonal tests. The influence of these core process parameters on the tensile strength of PETG parts is illustrated in Figure 4.

It should be noted that actual measurements showed the deviation between the specimen cross-sectional dimensions and standard values was within 0.05 mm. This negligible deviation meets engineering precision requirements; therefore, to simplify calculations, all tensile performance indicators were computed using standard cross-sectional dimensions. The tensile strength was calculated as follows:

$$R_m = \frac{F}{A_0} \tag{1}$$

where R_m is the tensile strength (MPa), F is the maximum tensile force (N), and A_0 is the initial cross-sectional area (mm^2).

Mean values were adopted for data analysis, with each experimental group consisting of three parallel specimens. Using the mean provides a more stable reflection of the overall experimental level and effectively avoids the lack of representativeness of the median in small sample sizes. Furthermore, this approach achieves reliable characterization of data laws without requiring excessively large samples, thereby enhancing experimental efficiency and economy.

According to the results in Figure 4, the tensile strength of PETG parts generally shows an increasing trend with increasing infill density, perimeter shells, and printing temperature, and also shows a gradual improvement with increasing layer height. As shown in Figure 4a, the strength increases gradually at low infill densities due to the presence of large internal pores; however, in the medium-to-high range, the pores diminish and provide enhanced structural support, leading to a significant increase in tensile strength. Figure 4b indicates that as layer height increases, the total number of layers decreases, thereby reducing the number of interlayer fusion interfaces and the risk of defects, thereby providing stronger structural support and significantly enhancing tensile strength. However, in actual fabrication, although specimens with a 0.25 mm layer height formed successfully, those at 0.3 mm (not shown) exhibited poor surface quality and inadequate interlayer fusion, failing to meet engineering requirements for appearance and precision.

In Figure 4c, when the number of perimeter shells is insufficient, the structural integrity of the specimen shell is compromised, failing to form an effective load-bearing structure and resulting in significantly weakened tensile capacity. Figure 4d demonstrates a positive correlation between printing temperature and tensile strength. The strength increases most rapidly between 230 and 240 °C, primarily because the filament is insufficiently melted at 230 °C, leading to weak interlayer bonding. As the temperature rises to 240 °C, the improved fluidity of the PETG

melt facilitates more thorough interlayer fusion. Beyond 240 °C, although the strength continues to rise slightly, the rate of improvement plateaus as interlayer bonding reaches saturation.

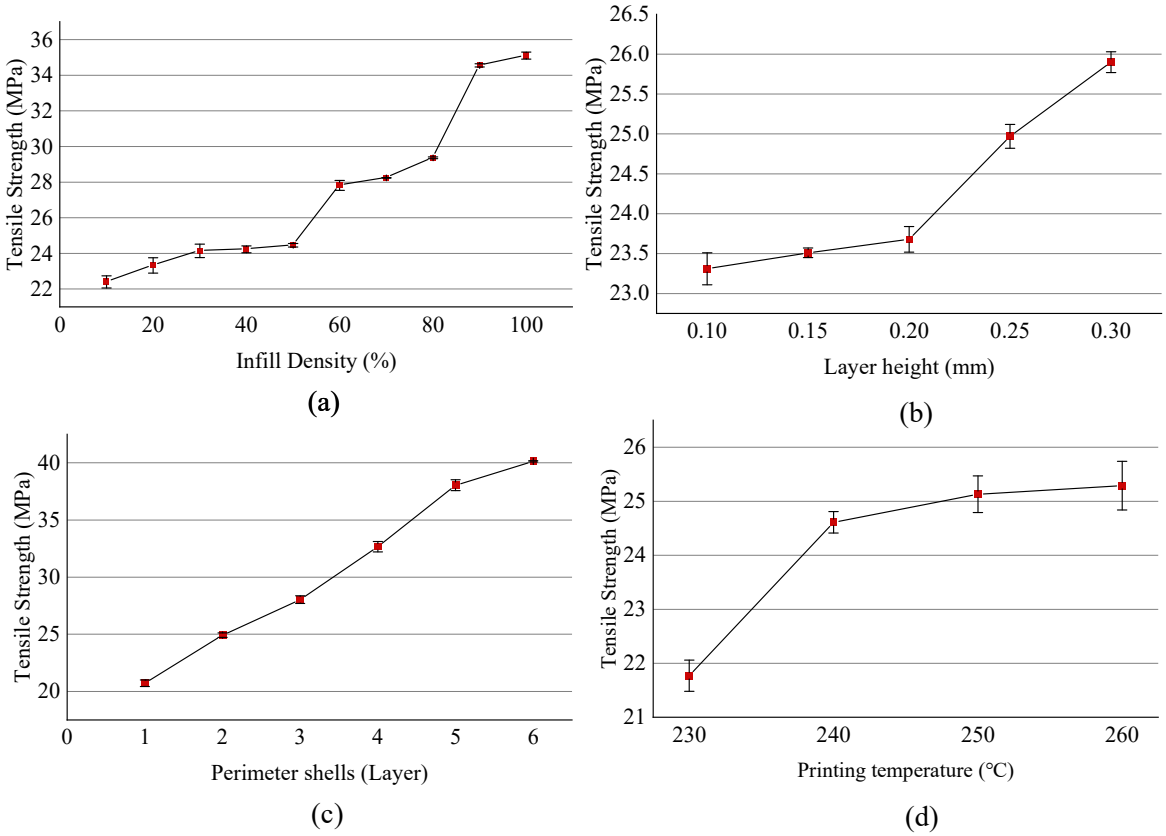

Figure 4. Effects of process parameters on tensile strength of PETG printed parts. (**a**) Infill density; (**b**) Layer height; (**c**) Perimeter shells; (**d**) Printing temperature.

3.2. Taguchi-OA experiment

Given that single-factor experiments cannot fully reflect the comprehensive effects under multi-parameter coupling, this study further utilized a Taguchi orthogonal array (Taguchi-OA) for multi-factor synergistic analysis. This method ensures a balanced distribution of parameter levels and allows for the efficient identification of influence laws using a reduced number of experimental runs [29,40]. Subsequently, Analysis of Variance (ANOVA) was used to identify the optimal process combination that balances tensile performance and manufacturing efficiency for PETG parts.

To balance the influence of various parameters, the rational ranges were determined based on single-factor results and relevant literature, as detailed in Table 1.

Table 1. Experimental factors and levels.

Levels	A	B	C	D	E
	Infill Density (%)	**Layer Height (mm)**	**Infill Pattern**	**Perimeter Shells (Layer)**	**Printing Temperature (°C)**
1	20	0.1	Grid	2	230
2	40	0.15	Honeycomb	3	240
3	60	0.2	Spiral	4	250
4	80	0.25	Lines	5	260

The selection criteria for each level were as follows: infill density was selected uniformly across the medium-to-high strength range; the layer height of 0.3 mm was excluded due to poor molding quality; four representative infill patterns—Grid, Honeycomb, Spiral, and Lines—were chosen; the 1-layer perimeter shell setting was excluded due to low mechanical strength; and the printing temperature levels were evenly distributed within the manufacturer-recommended range of 230–260 °C.

Following the Taguchi method, an $L_{16}(4^5)$ orthogonal array was designed based on the five selected parameters. To ensure statistical reliability, three replicate specimens were prepared for each parameter set, leading

to a total of 48 tensile tests. The experimental evaluation involved three key metrics: tensile strength, printing time, and material usage efficiency (MUE). This multi-metric strategy allowed a comprehensive analysis of the trade-offs among these indicators.

(1) Tensile Strength (MPa): Tensile Strength was adopted as the primary mechanical performance indicator, representing the maximum engineering stress sustained by the specimen before plastic deformation.

(2) Printing Time (s): Actual printing time can be affected by platform movement, printer preheating, filament flow calibration, and temperature stabilization, leading to minor fluctuations. To ensure the data are unified, comparable, and easy to calculate, this study utilized printing times estimated by the slicer software, excluding additional auxiliary time during the actual printing process.

(3) Material Usage Efficiency (MUE, mm^3/g): MUE was calculated as the ratio of the printed part volume to the mass of filament consumed, providing a quantitative measure of resource utilization efficiency:

$$MUE = \frac{V_p}{m_c} \tag{2}$$

where V_p is defined as the nominal envelope volume of the printed part (mm^3), which remains constant as a standardized reference regardless of internal porosity, and m_c is the total filament mass (g).

Table 2 summarizes the complete tensile test results of 16 groups of PETG specimens from the Taguchi experiment based on the $L_{16}(4^5)$ orthogonal array. The data in the table are the average test results for parallel specimens in each group, covering three response evaluation indicators: tensile strength, printing time, and MUE.

Table 2. Tensile test results of PETG material specimens from Taguchi-OA experiment L16 (4^5).

No.	Infill Density (%)	Layer Height (mm)	Infill Pattern	Perimeter Shells (Layer)	Printing Temperature (°C)	Tensile Strength (MPa)	Printing Time (s)	Material Usage Efficiency (mm^3/g)
1	1	1	1	1	1	22.71	348	1271.4
2	1	2	2	2	2	29.37	448	1102.5
3	1	3	3	3	3	34.7	353	1066.2
4	1	4	4	4	4	39.29	319	975.6
5	2	1	2	3	4	32.34	750	960.9
6	2	2	1	4	3	37.62	433	943.5
7	2	3	4	1	2	25.84	357	1088.4
8	2	4	3	2	1	32.34	349	1018.8
9	3	1	3	4	2	34.82	698	920.1
10	3	2	4	3	1	36.38	488	912.6
11	3	3	1	2	4	30.49	387	968.1
12	3	4	2	1	3	29.64	462	934.5
13	4	1	4	2	3	34.15	720	860.8
14	4	2	3	1	4	32.14	747	914.8
15	4	3	2	4	1	38.64	522	857.4
16	4	4	1	3	2	35.5	367	885.7

4. Results and Discussion

4.1. Analysis of Variance

ANOVA is a statistical method used to evaluate the differences between predicted values and experimental observations. Based on the aforementioned orthogonal test results, ANOVA was first performed on the experimental data to quantitatively evaluate the significance of each process parameter on the three response indicators and to establish corresponding prediction models. As shown in the residual plots in Figure 5, the residuals for the three response values approximately follow a normal distribution, satisfying the normality assumption required for ANOVA.

In the ANOVA, factors A, B, and D were treated as continuous variables. To ensure model parsimony and capture the predominant global trends, they were modeled as linear terms with a df of 1, following established methodologies [41,42]. Conversely, the printing temperature was set as a discrete variable (df = 3) to accurately capture its distinct non-linear sensitivity, which reflects the complex thermal bonding mechanisms observed in the preliminary experiments.

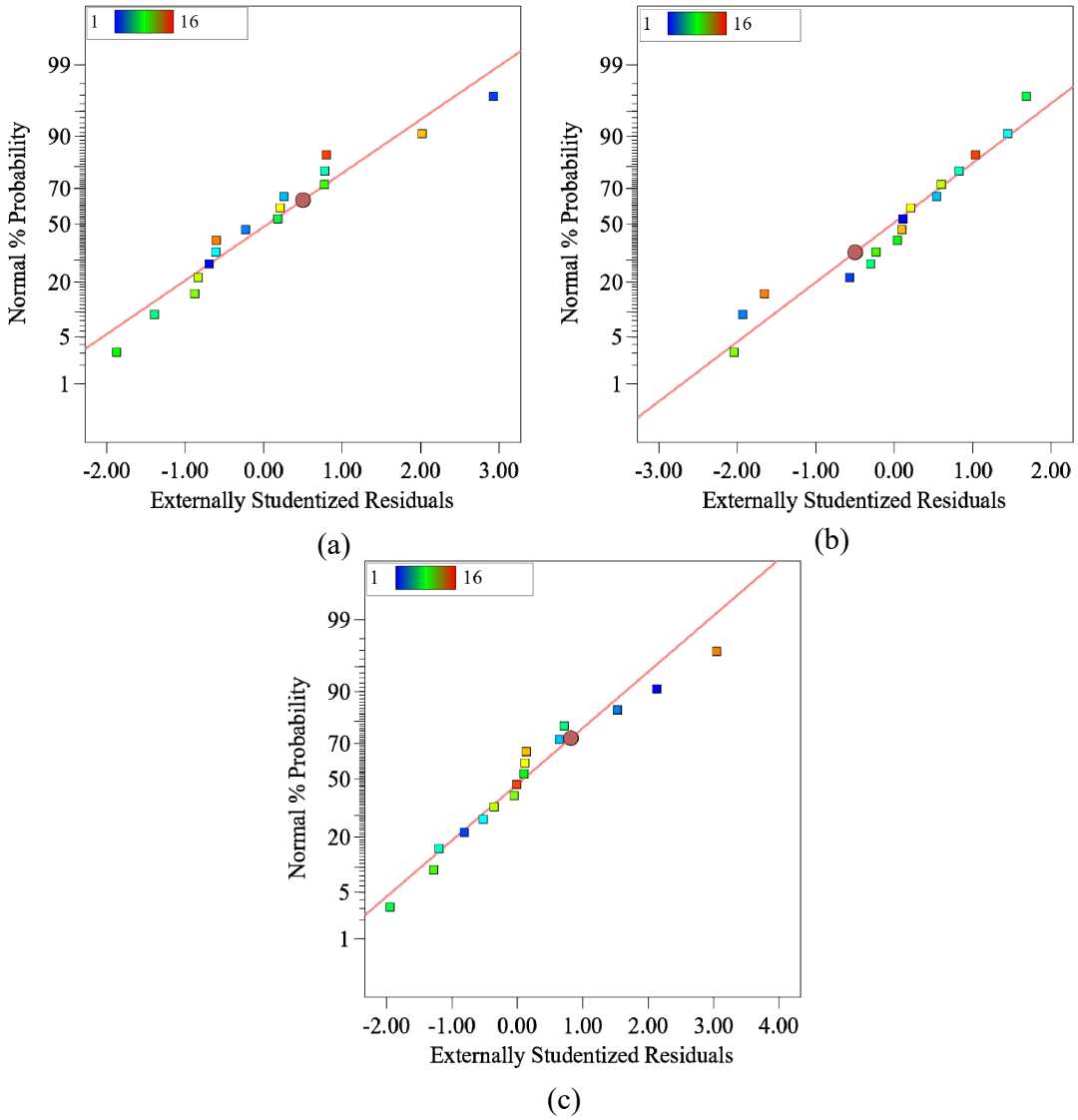

Figure 5. Residual plots: (**a**) Tensile Strength; (**b**) Printing Time; (**c**) Material Usage Efficiency.

Subsequently, the desirability function method was employed to determine the optimal process parameters, aiming to synergistically enhance tensile strength while minimizing printing costs. The analysis revealed intrinsic trade-offs between the response variables: maximizing tensile strength necessitated higher infill density and additional perimeter shells, which consequently increased printing time and material consumption. All predictive models demonstrated high statistical significance ($p < 0.01$). Detailed ANOVA results for each response are summarized in Table 3, providing a clear illustration of how each process parameter governs the respective performance indicators.

Parameter effect analyses were performed separately for each response indicator, and the top three process parameters with the greatest influence on each indicator were selected as core factors for further investigation. The main effect plots of key parameters derived from the orthogonal experimental results are presented in Figure 6, which clearly reveal the single-factor influence laws of infill density, layer height, infill pattern, number of perimeter shells, and printing temperature on each response indicator.

Regarding tensile strength, the number of perimeter shells shows an extremely significant positive correlation, with strength increasing considerably as the number rises from 2 to 5. This is because the perimeter shells act as a load-bearing skeleton for the specimen, effectively inhibiting the propagation of internal infill pores under tensile load and enhancing overall structural integrity. Infill density also presents a significant positive correlation, where tensile strength increases linearly as density rises from 20% to 80%, as higher density reduces internal porosity while increasing the effective load-bearing cross-sectional area and structural compactness. In contrast, infill pattern, layer height, and printing temperature have no significant impact on tensile strength within the tested range, indicating that tensile strength is determined by the overall structural configuration rather than being dominated by a single factor.

Table 3. ANOVA results of response variables.

Response Indicator	Source	Sum of Squares	df	Mean Square	*F*-Value	*p*-Value	
Tensile Strength	Model	289.78	9	32.20	11.10	0.0042	significant
	A	26.76	1	26.76	9.22	0.0229	
	B	13.13	1	13.13	4.53	0.0775	
	C	13.17	3	4.39	1.51	0.3042	
	D	220.08	1	220.08	75.86	0.0001	
	E	16.64	3	5.55	1.91	0.2289	
	Residual	17.41	6	2.90			
	Cor Total	307.19	15				
Printing Time	**Source**	**Sum of Squares**	**df**	**Mean Square**	***F*-Value**	***p*-Value**	
	Model	3.566×10^5	9	39,627.61	21.73	0.0007	significant
	A	98,701.25	1	98,701.25	54.12	0.0003	
	B	1.579×10^5	1	1.579×10^5	86.57	<0.0001	
	C	67,134.50	3	22,378.17	12.27	0.0057	
	D	649.80	1	649.80	0.3563	0.5724	
	E	32,276.50	3	10,758.83	5.90	0.0319	
	Residual	10,942.50	6	1823.75			
	Cor Total	3.676×10^5	15				
Material Usage Efficiency	**Source**	**Sum of Squares**	**df**	**Mean Square**	***F*-Value**	***p*-Value**	
	Model	1.681×10^5	9	18,676.96	16.11	0.0015	significant
	A	1.101×10^5	1	1.101×10^5	94.94	<0.0001	
	B	2990.24	1	2990.24	2.58	0.1594	
	C	8280.03	3	2760.01	2.38	0.1684	
	D	34,540.52	1	34,540.52	29.79	0.0016	
	E	12,220.97	3	4073.66	3.51	0.0890	
	Residual	6955.91	6	1159.32			
	Cor Total	1.750×10^5	15				

Tensile Strength: $R^2 = 0.94$; Adjusted $R^2 = 0.85$; Adeq Precision = 11.85. Printing Time: $R^2 = 0.97$; Adjusted $R^2 = 0.92$; Adeq Precision = 12.94. Material Usage Efficiency: $R^2 = 0.96$; Adjusted $R^2 = 0.90$; Adeq Precision = 15.79.

For printing time, both layer height and infill density are extremely significant influencing factors. Printing time decreases sharply with an increase in layer height from 0.1 mm to 0.25 mm, showing a negative correlation. This is due to the fact that larger layer heights result in fewer total layers and shorter extrusion paths. Conversely, a higher infill density necessitates more nozzle travel paths, leading to a significant prolongation of printing time. Additionally, infill pattern and printing temperature exert significant effects, whereas the number of perimeter shells has no significant influence.

For material usage efficiency, it is significantly negatively regulated by infill density and the number of perimeter shells. The molding volume per unit mass decreases substantially with an increase in these two parameters, indicating that higher infill densities and shell counts consume more filament, leading to increased material usage per unit volume and a decline in overall MUE. Layer height, infill pattern, and printing temperature show no significant effects on MUE.

The above main effect analysis reveals significant trade-offs among the parameters: increasing infill density and perimeter shells improves mechanical performance but reduces material utilization efficiency and prolongs printing time. Increasing layer height shortens printing time, and statistical results confirm that it does not significantly compromise tensile strength. These interdependent constraints provide a clear direction and theoretical basis for subsequent multi-objective parameter optimization.

To further reveal the coupling mechanism of key process parameters, interaction plots were adopted to analyze the synergistic effects of critical parameters on printing performance. Figure 7 presents the interaction effects of core parameters on the three response variables. Subplot (a) shows the interactive influence on tensile strength: strength increases monotonically with rising infill density, and a greater number of perimeter shells leads to higher strength, indicating that the two parameters synergistically enhance mechanical performance. Subplot (b) displays the interaction between infill density and perimeter shells on printing time: an increase in either parameter results in a significant prolongation of printing time, and the time-cost increment caused by infill density is more pronounced at higher shell counts. Subplot (c) illustrates the interaction on MUE: efficiency decreases linearly with increasing infill density, and the decline becomes more significant with more perimeter shells, meaning that the two parameters jointly exacerbate material consumption. These interaction effects clarify the inherent trade-offs between mechanical performance, printing efficiency, and material utilization, laying the foundation for constructing prediction models and implementing multi-objective optimization.

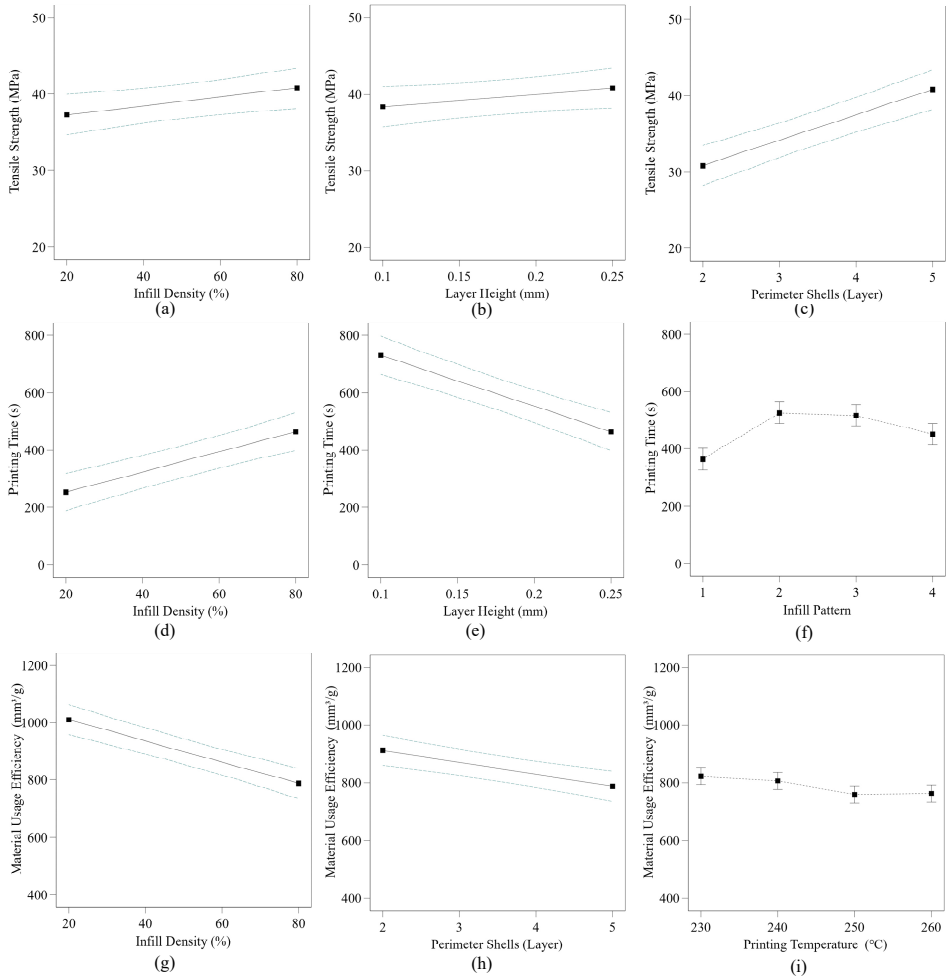

Figure 6. Main effect plots of key parameters for each indicator: tensile strength (**a**–**c**), printing time (**d**–**f**), and material usage efficiency (**g**–**i**).

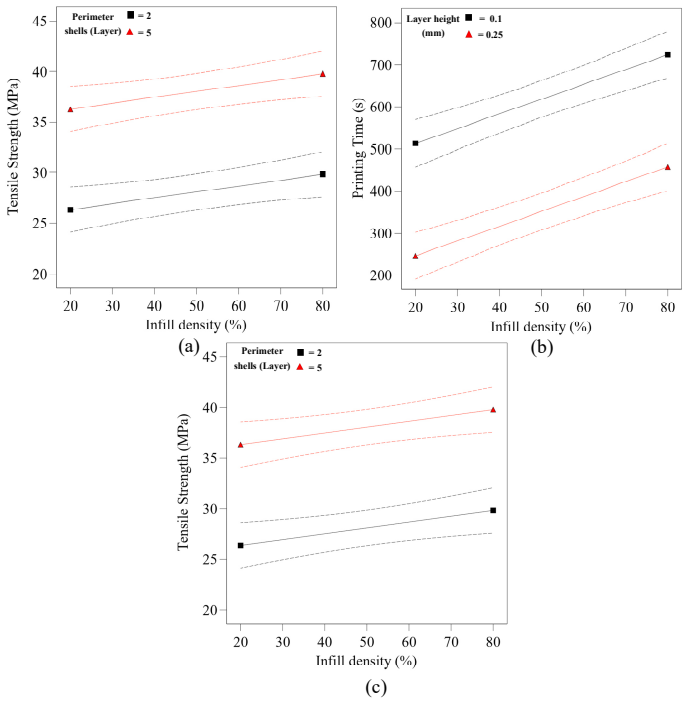

Figure 7. Interaction plots of key process parameters on the three response indicators: (**a**) Tensile Strength; (**b**) Printing Time; (**c**) Material Usage Efficiency.

4.2. Multi-Objective Optimization Methodology

Based on the inherent parameter coupling mechanisms elucidated through the interaction analysis, a multiple linear regression approach was executed using Design-Expert 13 software. This facilitated the construction of empirical prediction models that establish the functional relationship between MEX process parameters and the tripartite response indicators: tensile strength, printing time, and material usage efficiency (MUE). The refined regression equations are presented as follows:

$$Y_1 = 40.80 + 3.47A + 2.43B - 1.29C_1 - 0.38C_2 + 0.63C_3 + 9.95D + 0.29E_1 + 0.17E_2 - 0.34E_3 \quad (3)$$

$$Y_2 = 464.90 + 210.75A - 266.55B - 100.50C_1 + 61.25C_2 + 52.50C_3 + 17.10D + 19.83E_1 + 4.50E_2 + 2.53E_3 \quad (4)$$

$$Y_3 = 788.13 - 222.55A - 36.68B + 37.09C_1 - 16.26C_2 - 0.11C_3 - 124.67D - 11.43E_1 + 4.87E_2 + 4.18E_3 \quad (5)$$

In the equations, Y_1 denotes tensile strength (MPa), Y_2 denotes printing time (s), and Y_3 denotes material usage efficiency (mm^3/g); A represents infill density (%), B represents layer height (mm), and D represents the number of perimeter shells. are dummy variables for the infill pattern, representing Grid, Honeycomb, and Spiral, respectively, with Lines serving as the reference group. are dummy variables for printing temperature, representing 230 °C, 240 °C, and 250 °C, respectively, with 260 °C as the reference group. The absolute value of each coefficient in the equations reflects the magnitude of the influence of the corresponding parameter on the response indicator. At the same time, the sign indicates whether the effect is a promotion or an inhibition.

Based on the influence of the above parameters on each response indicator, an optimization model targeting multiple response indicators was constructed. The specific optimization objectives and constraints are as follows:

Objective function:

$$\begin{cases} Max\ Y_1 = f(A,B,C,D,E) \\ Min\ Y_2 = f(A,B,C,D,E) \\ Max\ Y_3 = f(A,B,C,D,E) \end{cases}$$

Subject to (*S.T.*):

$$S.T. \begin{cases} 20 \le A \le 80 \\ 0.1 \le B \le 0.25 \\ 1 \le C \le 4 \\ 2 \le D \le 5 \\ 230 \le E \le 260 \end{cases}$$

In the formulation, A is infill density (%), B is layer height (mm), C is infill pattern type, D is the number of perimeter shells, and E is printing temperature (°C).

Combined with the solution results of the aforementioned multi-objective optimization model, the optimal process parameter combination was finally determined by comprehensively balancing the mechanical performance, printing time, and material usage efficiency of MEX-printed PETG components. The identified parameters are as follows: an infill density of 52%, a layer height of 0.25 mm, a grid infill pattern, 5 perimeter shells, and a printing temperature of 250 °C. Notably, the infill density of 52% was derived from continuous numerical optimization and subsequently rounded to the nearest integer for practical printing implementation; this adjustment is considered to have no significant impact on the final printing outcomes. Under these optimized conditions, the model predicts a tensile strength of 39.01 MPa, a printing time of 277 s, and a material usage efficiency of 900.4 mm^3/g.

4.3. Model Validation and Analysis

To verify the reliability and engineering practicability of the established regression model and the obtained process parameters, PETG specimens were fabricated via MEX printing, and tensile performance verification tests were conducted based on the aforementioned optimal process parameter combination. The measured tensile strength was 38.81 MPa, with a relative deviation of less than 1% compared with the model-predicted value of 39.01 MPa. The measured material usage efficiency (MUE) was 915 mm^3/g, which is in good agreement with the predicted value of 900.4 mm^3/g. Although the measured printing time (291 s) was slightly higher than the predicted value (277 s) with a relative deviation of 5.05%, this discrepancy remains within the acceptable engineering range. The deviation is primarily attributed to the printer's acceleration and deceleration phases, as well as the minor latency in heating stabilization, which are not fully captured by the slicer's kinematic model. Despite this, the results do not compromise the application value of the optimal parameter combination, as detailed in Table 4.

Table 4. Model validation results.

Category	Tensile Strength (MPa)	Printing Time (s)	Material usage Efficiency (mm^3/g)
Predicted value	39.01	277	900.4
Measured value	38.81	291	915
Relative deviation	0.51%	5.05%	1.62%

Note: The relative deviations are all within the acceptable engineering range, confirming the reliability of the prediction model.

Simultaneously, to verify the effectiveness of the optimization scheme, a control group was prepared using the default slicer software parameters: 0.2 mm layer height, 240 °C printing temperature, 2 perimeter shells, 20% infill density, and a grid infill pattern. The mechanical performance comparison between the optimized and default specimens is shown in Figure 8.

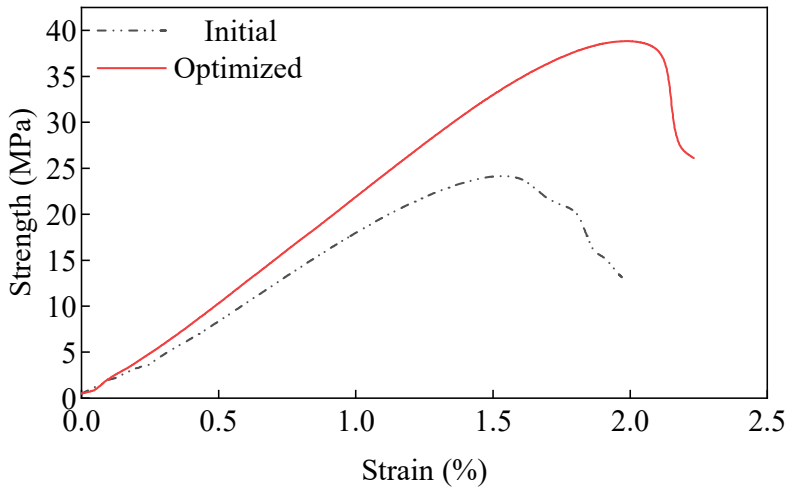

Figure 8. Tensile performance comparison before and after optimization.

As shown in the stress-strain curves in Figure 8, the tensile strength of the specimen before optimization was approximately 24.5 MPa with a low elongation at break. The curve dropped rapidly after reaching the peak, exhibiting typical brittle fracture characteristics. In contrast, the optimized specimen's tensile strength increased to approximately 39 MPa, accompanied by a significantly higher elongation at break. The curve presented a more pronounced plastic yielding stage, indicating that the specimen underwent more thorough plastic deformation before failure.

From the perspective of fracture mechanisms, the default parameters (20% infill density, 2 shells) resulted in large internal pores and structural discontinuities, preventing the formation of an effective support structure. Under tensile load, stress is concentrated at weak interlayer interfaces and defect sites, leading to rapid crack propagation along the interfaces and resulting in brittle fracture dominated by interfacial delamination. Conversely, the optimized parameters significantly improved the process by enhancing interlayer fusion. Increasing the infill density (52%) improved the overall compactness and reduced defects caused by excessive porosity. Consequently, the load-bearing capacity was shared by both the infill matrix and the perimeter shells, allowing the material to utilize its full tensile capacity. The fracture mode shifted to primarily ductile matrix fracture accompanied by minor interlayer shear failure, thus demonstrating the effectiveness and engineering applicability of the optimization strategy proposed in this study.

The analysis of the parameter coupling mechanism shows that infill density and perimeter shells synergistically improve tensile strength while simultaneously increasing printing time and material consumption; meanwhile, appropriately increasing layer height can significantly enhance printing efficiency without obviously weakening mechanical properties. This clearly reveals the inherent trade-offs among structural compaction, molding efficiency, and material consumption in the MEX process.

5. Conclusions

This study systematically investigated the influence of five pivotal process parameters—infill density, layer height, infill pattern, perimeter shells, and printing temperature—on the tensile strength, printing time, and material usage efficiency (MUE) of MEX-fabricated PETG parts. Based on Taguchi orthogonal design, Analysis of Variance (ANOVA), and multiple linear regression modeling, the individual effects, significance levels, and

coupling mechanisms of these parameters were comprehensively elucidated through the desirability function method. The results indicate that perimeter shells and infill density predominate the tensile strength, layer height governs the printing time, and infill density dictates the MUE. These findings reveal an inherent trade-off among mechanical performance, manufacturing efficiency, and material consumption. The main conclusions are as follows:

(1) This study established an intuitive and streamlined engineering evaluation framework by integrating MUE with printing time. By avoiding overly complex or abstract metrics, this approach aligns closely with practical industrial requirements, providing a convenient and pragmatic quantitative basis for the high-efficiency, low-cost manufacturing of the MEX process.

(2) By concurrently incorporating tensile strength, printing time, and MUE into a multi-objective optimization framework, this study effectively addresses the limitations of existing literature, which often focuses solely on single-objective mechanical optimization. This approach reconciles the previously fragmented analyses, achieving a synergistic enhancement of the mechanical performance, manufacturing efficiency, and economic viability of PETG components.

(3) High-precision multiple linear regression models were constructed based on orthogonal testing and ANOVA, with the multi-objective optimization solved via the desirability function method. Experimental validation confirmed that the identified optimal process configuration facilitates a substantial improvement in mechanical performance without necessitating excessively high infill densities.

(4) The underlying influence mechanisms and coupling laws of key parameters were revealed: while perimeter shells and infill density are the primary determinants of tensile strength, layer height serves as the core driver of printing efficiency. Furthermore, an increase in infill density significantly undermines the MUE. Post-optimization analysis showed that the fracture mode transitioned from brittle interlayer delamination to ductile matrix fracture, thereby elucidating the intrinsic correlations between process parameters, microstructure, and mechanical behavior.

In summary, this study systematically executed a multi-objective optimization of the MEX process for PETG materials. It proposed and defined the quantitative metric of MUE, developed robust predictive models, and completed a thorough analysis of parameter coupling alongside the determination of optimal parameters. These findings provide a solid theoretical foundation and technical support for the collaborative optimization of performance, efficiency, and cost in MEX-printed PETG components, contributing significantly to the development of cost-controllable additive manufacturing. Nevertheless, certain limitations remain; this study focused exclusively on virgin PETG material using a 0.4 mm nozzle, without considering variations in nozzle diameters or the influence of material moisture. Subsequent research may expand into multi-specification nozzles and material state conditioning to further refine the MEX process theoretical framework.

Author Contributions

T.L.: conceptualization, methodology, formal analysis, data curation, writing—original draft preparation; H.W.: validation, investigation; Y.L.: software, visualization; Y.W.: resources; H.L.: investigation, validation; B.T.: writing—reviewing and editing; Y.P.: methodology, visualization; L.L.: supervision, project administration, funding acquisition. All authors have read and agreed to the published version of the manuscript.

Funding

This research was funded by the Science and Technology Research Program of Chongqing Municipal Education Commission (No. KJQN202301242 and KJQN202301229).

Institutional Review Board Statement

Not applicable.

Informed Consent Statement

Not applicable.

Data Availability Statement

All data supporting the findings of this study are included in the manuscript. The raw data are available from the corresponding author upon reasonable request.

Conflicts of Interest

The authors declare no competing interests.

Use of AI and AI-Assisted Technologies

No AI tools were utilized for this paper.

References

1. Jandyal, A.; Chaturvedi, I.; Wazir, I.; et al. 3D Printing—A Review of Processes, Materials and Applications in Industry 4.0. *Sustain. Oper. Comput.* **2022**, *3*, 33–42. https://doi.org/10.1016/j.susoc.2021.09.004.
2. Bogue, R. 3D Printing: The Dawn of a New Era in Manufacturing? *Assem. Autom.* **2013**, *33*, 307–311. https://doi.org/10.1108/AA-06-2013-055.
3. Seyedzavvar, M.; Boğa, C. Investigation on the Effects of Printing Pattern on the Load Carrying Capacity of 3D Printed U-Notched Samples. *Meccanica* **2022**, *57*, 1575–1590. https://doi.org/10.1007/s11012-022-01514-8.
4. Kechagias, J.; Zaoutsos, S. Effects of 3D-Printing Processing Parameters on FFF Parts' Porosity: Outlook and Trends. *Mater. Manuf. Process.* **2024**, *39*, 804–814. https://doi.org/10.1080/10426914.2024.2304843.
5. Graziosi, S.; Faludi, J.; Stanković, T.; et al. A Vision for Sustainable Additive Manufacturing. *Nat. Sustain.* **2024**, *7*, 698–705. https://doi.org/10.1038/s41893-024-01313-x.
6. Rani, S.; Jining, D.; Shoukat, K.; et al. A Human–Machine Interaction Mechanism: Additive Manufacturing for Industry 5.0—Design and Management. *Sustainability* **2024**, *16*, 4158. https://doi.org/10.3390/su16104158.
7. Ma, T.; Zhang, Y.; Ruan, K.; et al. Advances in 3D Printing for Polymer Composites: A Review. *InfoMat* **2024**, *6*, e12568. https://doi.org/10.1002/inf2.12568.
8. Chekkaramkodi, D.; Jacob, L.; C, M.S.; et al. Review of Vat Photopolymerization 3D Printing of Photonic Devices. *Addit. Manuf.* **2024**, *86*, 104189. https://doi.org/10.1016/j.addma.2024.104189.
9. Ng, W.L.; Goh, G.L.; Goh, G.D.; et al. Progress and Opportunities for Machine Learning in Materials and Processes of Additive Manufacturing. *Adv. Mater.* **2024**, *36*, 2310006. https://doi.org/10.1002/adma.202310006.
10. Lee, J.-Y.; An, J.; Chua, C.K. Fundamentals and Applications of 3D Printing for Novel Materials. *Appl. Mater. Today* **2017**, *7*, 120–133. https://doi.org/10.1016/j.apmt.2017.02.004.
11. Shahrubudin, N.; Lee, T.C.; Ramlan, R. An Overview on 3D Printing Technology: Technological, Materials, and Applications. *Procedia Manuf.* **2019**, *35*, 1286–1296. https://doi.org/10.1016/j.promfg.2019.06.089.
12. Ngo, T.D.; Kashani, A.; Imbalzano, G.; et al. Additive Manufacturing (3D Printing): A Review of Materials, Methods, Applications and Challenges. *Composites Part B Eng.* **2018**, *143*, 172–196. https://doi.org/10.1016/j.compositesb.2018.02.012.
13. Liu, Z.; Zhang, M.; Bhandari, B.; et al. 3D Printing: Printing Precision and Application in Food Sector. *Trends Food Sci. Technol.* **2017**, *69*, 83–94. https://doi.org/10.1016/j.tifs.2017.08.018.
14. Wang, X.; Huang, L.; Li, Y.; et al. Research Progress in Polylactic Acid Processing for 3D Printing. *J. Manuf. Process.* **2024**, *112*, 161–178. https://doi.org/10.1016/j.jmapro.2024.01.038.
15. Mudau, M.; Adebo, O.A. Three Dimensional (3D)-Printed Foods: A Review of Recent Advances in Their Ingredients, Printing Techniques, Food Printers, Post-Processing Methods, Consumer Acceptance and Safety. *J. Food Process Eng.* **2024**, *47*, e14621. https://doi.org/10.1111/jfpe.14621.
16. Sharma, R.; Chandra Nath, P.; Kumar Hazarika, T.; et al. Recent Advances in 3D Printing Properties of Natural Food Gels: Application of Innovative Food Additives. *Food Chem.* **2024**, *432*, 137196. https://doi.org/10.1016/j.foodchem.2023.137196.
17. Daminabo, S.C.; Goel, S.; Grammatikos, S.A.; et al. Fused Deposition Modeling-Based Additive Manufacturing (3D Printing): Techniques for Polymer Material Systems. *Mater. Today Chem.* **2020**, *16*, 100248. https://doi.org/10.1016/j.mtchem.2020.100248.
18. MacDonald, E.; Wicker, R. Multiprocess 3D Printing for Increasing Component Functionality. *Science* **2016**, *353*, aaf2093. https://doi.org/10.1126/science.aaf2093.
19. Roschli, A.; Post, B.K.; Wang, P.; et al. The Cost of Scaling Up in Large-Format Additive Manufacturing. *3D Print. Addit. Manuf.* **2025**, 1–10. https://doi.org/10.1089/3dp.2023.0112.
20. Kristiawan, R.B.; Imaduddin, F.; Ariawan, D.; et al. A Review on the Fused Deposition Modeling (FDM) 3D Printing: Filament Processing, Materials, and Printing Parameters. *Open Eng.* **2021**, *11*, 639–649. https://doi.org/10.1515/eng-2021-0063.
21. Equbal, A.; Murmu, R.; Kumar, V.; et al. A Recent Review on Advancements in Dimensional Accuracy in Fused Deposition Modeling (FDM) 3D Printing. *AIMS Mater. Sci.* **2024**, *11*, 950–990. https://doi.org/10.3934/matersci.2024046.
22. Wickramasinghe, S.; Do, T.; Tran, P. FDM-Based 3D Printing of Polymer and Associated Composite: A Review on Mechanical Properties, Defects and Treatments. *Polymers* **2020**, *12*, 1529. https://doi.org/10.3390/polym12071529.
23. Popović, M.; Pjević, M.; Milovanović, A.; et al. Printing Parameter Optimization of PLA Material Concerning Geometrical Accuracy and Tensile Properties Relative to FDM Process Productivity. *J. Mech. Sci. Technol.* **2023**, *37*, 697–706. https://doi.org/10.1007/s12206-023-0113-6.

24. Özen, A.; Auhl, D.; Völlmecke, C.; et al. Optimization of Manufacturing Parameters and Tensile Specimen Geometry for Fused Deposition Modeling (FDM) 3D-Printed PETG. *Materials* **2021**, *14*, 2556. https://doi.org/10.3390/ma14102556.
25. Lakshman Sri, S.V.; Karthick, A.; Dinesh, C. Evaluation of Mechanical Properties of 3D Printed PETG and Polyamide (6) Polymers. *Chem. Phys. Impact* **2024**, *8*, 100491. https://doi.org/10.1016/j.chphi.2024.100491.
26. Vidakis, N.; Petousis, M.; Velidakis, E.; et al. On the Strain Rate Sensitivity of Fused Filament Fabrication (FFF) Processed PLA, ABS, PETG, PA6, and PP Thermoplastic Polymers. *Polymers* **2020**, *12*, 2924. https://doi.org/10.3390/polym12122924.
27. Nugroho, A.; Ardiansyah, R.; Rusita, L.; et al. Effect of Layer Thickness on Flexural Properties of PLA (PolyLactid Acid) by 3D Printing. *J. Phys. Conf. Ser.* **2018**, *1130*, 012017. https://doi.org/10.1088/1742-6596/1130/1/012017.
28. Loskot, J.; Jezbera, D.; Loskot, R.; et al. Influence of Print Speed on the Microstructure, Morphology, and Mechanical Properties of 3D-Printed PETG Products. *Polym. Test.* **2023**, *123*, 108055. https://doi.org/10.1016/j.polymertesting.2023.108055.
29. Valvez, S.; Silva, A.P.; Reis, P.N.B. Optimization of Printing Parameters to Maximize the Mechanical Properties of 3D-Printed PETG-Based Parts. *Polymers* **2022**, *14*, 2564. https://doi.org/10.3390/polym14132564.
30. Bembenek, M.; Kowalski, Ł.; Kosoń-Schab, A. Research on the Influence of Processing Parameters on the Specific Tensile Strength of FDM Additive Manufactured PET-G and PLA Materials. *Polymers* **2022**, *14*, 2446. https://doi.org/10.3390/polym14122446.
31. Luo, H.; Tan, Y.; Zhang, F.; et al. Selectively Enhanced 3D Printing Process and Performance Analysis of Continuous Carbon Fiber Composite Material. *Materials* **2019**, *12*, 3529. https://doi.org/10.3390/ma12213529.
32. Kechagias, J.; Zaoutsos, S. Optimization Window of Printing Parameters for Specific Strength and Energy Consumption in PEEK Additive Manufacturing. *Mater. Manuf. Processes* **2026**, *41*, 229–236. https://doi.org/10.1080/10426914.2026.2613641.
33. Kantaros, A.; Katsantoni, M.; Ganetsos, T.; et al. The Evolution of Thermoplastic Raw Materials in High-Speed FFF/FDM 3D Printing Era: Challenges and Opportunities. *Materials* **2025**, *18*, 1220. https://doi.org/10.3390/ma18061220.
34. Napolitano, F.; Cozzolino, E.; Papa, I.; et al. Experimental Integrated Approach for Mechanical Characteristic Optimization of FDM-Printed PLA in an Energy-Saving Perspective. *Int. J. Adv. Manuf. Technol.* **2022**, *121*, 3551–3565. https://doi.org/10.1007/s00170-022-09535-z.
35. Marșavina, L.; Vălean, C.; Mărghitaș, M.; et al. Effect of the Manufacturing Parameters on the Tensile and Fracture Properties of FDM 3D-Printed PLA Specimens. *Eng. Fract. Mech.* **2022**, *274*, 108766. https://doi.org/10.1016/j.engfracmech.2022.108766.
36. Saeimi Sadigh, M.A.; Safi Valilu, H.; Mohammadi, A.; et al. Auxetic Metamaterials Application: 3D Printing and Systematic Optimization of a Sandwich Panel Core for Maximum Energy Dissipation. *Iran J. Sci. Technol. Trans. Mech. Eng.* **2026**, *50*, 513–530. https://doi.org/10.1007/s40997-025-00950-7.
37. Warnung, L.; Estermann, S.-J.; Reisinger, A. Mechanical Properties of Fused Deposition Modeling (FDM) 3D Printing Materials. *RTe J.* **2018**, *15*, 1–10.
38. Somireddy, M.; Czekanski, A. Mechanical Characterization of Additively Manufactured Parts by FE Modeling of Mesostructure. *J. Manuf. Mater. Process.* **2017**, *1*, 18. https://doi.org/10.3390/jmmp1020018.
39. Collins, L.M.; Dziak, J.J.; Li, R. Design of Experiments with Multiple Independent Variables: A Resource Management Perspective on Complete and Reduced Factorial Designs. *Psychol. Methods* **2009**, *14*, 202–224. https://doi.org/10.1037/a0015826.
40. Tosi, G.; Mucchi, E.; d'Ippolito, R.; et al. Dynamic Behavior of Pumps: An Efficient Approach for Fast Robust Design Optimization. *Meccanica* **2015**, *50*, 2179–2199. https://doi.org/10.1007/s11012-015-0142-z.
41. Lanzotti, A.; Grasso, M.; Staiano, G.; et al. The Impact of Process Parameters on Mechanical Properties of Parts Fabricated in PLA with an Open-Source 3-D Printer. *Rapid Prototyp. J.* **2015**, *21*, 604–617. https://doi.org/10.1108/RPJ-09-2014-0135.
42. Rayegani, F.; Onwubolu, G.C. Fused Deposition Modelling (FDM) Process Parameter Prediction and Optimization Using Group Method for Data Handling (GMDH) and Differential Evolution (DE). *Int. J. Adv. Manuf. Technol.* **2014**, *73*, 509–519. https://doi.org/10.1007/s00170-014-5835-2.